PHYSICAL REVIEW B **90**, 054202 (2014)

Frozen light in a near-zero index metasurface

G. D'Aguanno,[1,*] N. Mattiucci,[1] M. J. Bloemer,[2] R. Trimm,[3] N. Aközbek,[1] and A. Alù[4]
[1]*AEgis Technologies, Inc.,410 Jan Davis Drive, Huntsville, Alabama 35806, USA*
[2]*Department of the Army, C. M. Bowden Laboratory, Redstone Arsenal, Alabama 35898, USA*
[3]*Miltec Corporation, 678 Discovery Drive, Huntsville, Alabama 35806, USA*
[4]*Department of Electrical and Computer Engineering, The University of Texas at Austin, Austin, Texas 78712, USA*
(Received 24 February 2014; revised manuscript received 29 June 2014; published 7 August 2014)

We discuss the nature of leaky modes with large phase velocity and an effective refractive index and group velocity near zero in planar arrays of subwavelength dielectric or metallic spheres far from their resonances. Large field enhancements with Q factors exceeding 10^{10} are theoretically predicted for these modes. Those theoretical findings may have important applications in optical switching and memories, quantum information processing, optical storage, and enhancement of optical nonlinearities. Preliminary experimental results at microwave frequencies qualitatively confirm these predictions.

DOI: 10.1103/PhysRevB.90.054202 PACS number(s): 42.25.Fx, 41.20.Jb, 42.79.Dj, 73.20.Mf

I. INTRODUCTION

The remarkably large velocity of light ($c \sim 3 \times 10^8$ m/s in vacuum) is of great benefit for various reasons: It allows us, for example, to get information about stars residing in remote places of the universe or makes possible the transmission of large amounts of data through optical fibers from one point of our planet to another in extremely short times. Yet, there are several instances in which it is beneficial to control and to reduce the speed of light propagation. For example, it is well known that efficient nonlinear light-matter interactions may be achieved when the product of the transition rate and the interaction time is large. Slowing down light increases its interaction time with the medium and therefore ultimately enhances the material's effective nonlinearities. In quantum information processing, slowing down light allows its storage for a sufficiently long time so to enable quantum operations. In information networks, it is highly desirable to use slow light for all-optical routing that temporarily stores data.

To date, the available methods to slow down light can be roughly divided into two broad categories [1]. The first relies on the excitation of intrinsic resonances in a medium, such as an atomic vapor or a crystal. Reduction of the group velocity of light pulses to 17 m/s in a Bose condensate of ultracold sodium atoms has been reported in Ref. [2]. Group velocity of 90 m/s in a hot rubidium gas has been demonstrated in Ref. [3], and 45 m/s in a Pr-doped Y_2SiO_5 crystal has been demonstrated in Ref. [4]. The effect involves the resonant interaction between a control and a signal beam, tuned such that quantum coherence is established between an excited state and two nearly degenerate ground states [2–4]. The second category relies on geometrical resonances created in artificial structures, whose refractive index is either modulated on a scale on the order of the incident wavelength (for example, as in photonic crystals [5] and Bragg gratings [6,7], etc.) or whose refractive index is modulated on a much finer scale (metamaterials [8]). Typical metamaterial solutions, however, generally depend on metallic structures and/or metallic inclusions [9], whose inherent losses may significantly hamper slow-light effects. In this paper, we use a rigorous Green's-function approach to show the existence of light modes sustained by thin metasurfaces made of subwavelength particles arranged in a periodic array that combine meta-material-like properties, such as an effective wavelength approaching infinity, i.e., an effective index close to zero, and slow-light properties but without the detrimental effects associated with metallic losses.

II. THEORETICAL MODEL

The generic structure under investigation is schematically represented in Fig. 1.

Following a Green's-function approach [10], under the dipole approximation, the induced dipole moment on the particles in the array can be written in the nondimensional mksa system ($\varepsilon_0 = \mu_0 = c = 1$) as

$$\text{TE}: \quad p_y = \frac{E_0}{\alpha^{-1} - k_0^2 \sum_{(p,q)\neq(0,0)} G_{yy}(x_p, y_q, z=0) e^{i k_{x,in} x_p}}, \tag{1a}$$

$$\text{TM}: \begin{cases} p_x = \dfrac{\sqrt{k_0^2\varepsilon_b - k_{x,in}^2}}{k_0 \varepsilon_b} \dfrac{H_0}{[\alpha^{-1} - k_0^2 \sum_{(p,q)\neq(0,0)} G_{xx}(x_p, y_q, z=0) e^{i k_{x,in} x_p}]}, \\ p_z = -\dfrac{k_{x,in}}{k_0 \varepsilon_b} \dfrac{H_0}{[\alpha^{-1} - k_0^2 \sum_{(p,q)\neq(0,0)} G_{zz}(x_p, y_q, z=0) e^{i k_{x,in} x_p}]}, \end{cases} \tag{1b}$$

where $k_{x,in} = k_b \sin\vartheta$ is the transverse momentum of the incident field as in Fig. 1, $k_b = n_b k_0$ is the background medium wave vector, $k_0 = 2\pi/\lambda$ is the vacuum wave vector, G_{xx}, G_{yy}, and G_{zz} are the diagonal elements of the single-particle dyadic Green's function $\hat{G} = (\hat{I} + k_b^{-2}\nabla\nabla) g(\rho)$ with $g(\rho) = (4\pi)^{-1} e^{i k_b \rho}/\rho$ and $\rho = \sqrt{x^2 + y^2 + z^2}$, and, finally, α is the single-particle polarizability coefficient including the correction term dictated by the optical theorem [11] $\alpha = [(4\pi r^3 \varepsilon_b \frac{\varepsilon_s - \varepsilon_b}{\varepsilon_s + 2\varepsilon_b})^{-1} - i \frac{k_b^3}{6\pi\varepsilon_b}]^{-1}$, where, with reference to Fig. 1, r is the particle radius, ε_s is its relative electric permittivity, and ε_b is the relative electric permittivity of the background medium. For an array that is periodic along the x and y directions and for an incident wave vector having a zero component along either the x or the y direction (in our case the incident wave vector has indeed no component along the y direction), it can be easily demonstrated that only the sum of the diagonal elements of the Green's tensor with the appropriate phase factors contribute to the effective polarizability

---

[*] Corresponding author: gdaguanno@aegistg.com; giuseppe.daguanno@us.army.mil

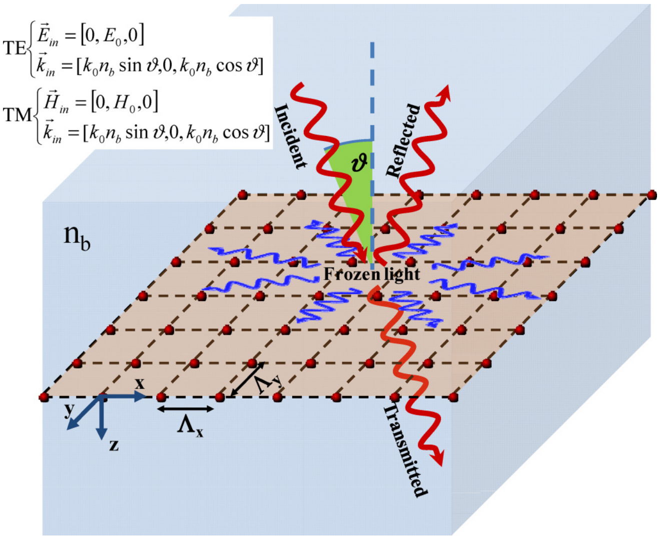

FIG. 1. (Color online) Periodic planar array ($z = 0$) of subwavelength spherical particles with radius r and relative electric permittivity ε_s embedded in a generic background medium with refractive index $n_b = (\varepsilon_b)^{1/2}$. Both transverse electric (TE) and transverse magnetic (TM) excitations are considered. The positions of the particles along the x and y axes are $x_p = p\Lambda_x$ and $y_q = q\Lambda_y$, respectively, with $(p,q) = 0,\pm1,\pm2,\ldots$.

of the array, whereas, for symmetry reasons, the nondiagonal elements add up to zero. For the numerical calculation, the slow convergent lattice sums in Eq. (1) have been converted into fast convergent sums using the Ewald method [12].

Once the dipole moment components (p_x,p_y,p_z) are calculated, the electromagnetic problem is formally solved, and by resorting to the periodic Green's function of the whole array, explicit expressions of the total electric field components can be calculated in terms of the sum of the incident and scattered fields as follows:

$$E_k(x,y,z) = E_{k,in} + E_{\text{scat}} \quad \text{with}$$
$$E_{\text{scat}} = \sum_{m,n} A^{(k)}_{m,n} e^{i(\alpha_m x + \beta_n y + k_{m,n}|z|)},$$
$$k = x,y,z, \qquad (2a)$$

where $\alpha_m = k_{x,in} + mG_x$ and $\beta_n = k_{y,in} + nG_y$ (in our case $k_{y,in} = 0$) are the generalized transverse wave vectors of the array [$G_x = 2\pi/\Lambda_x$ and $G_y = 2\pi/\Lambda_y$ are the reciprocal lattice vectors, $(m,n) = 0,\pm1,\pm2,\ldots$], $k_{m,n} = \sqrt{k_0^2\varepsilon_b - \alpha_m^2 - \beta_n^2}$, and

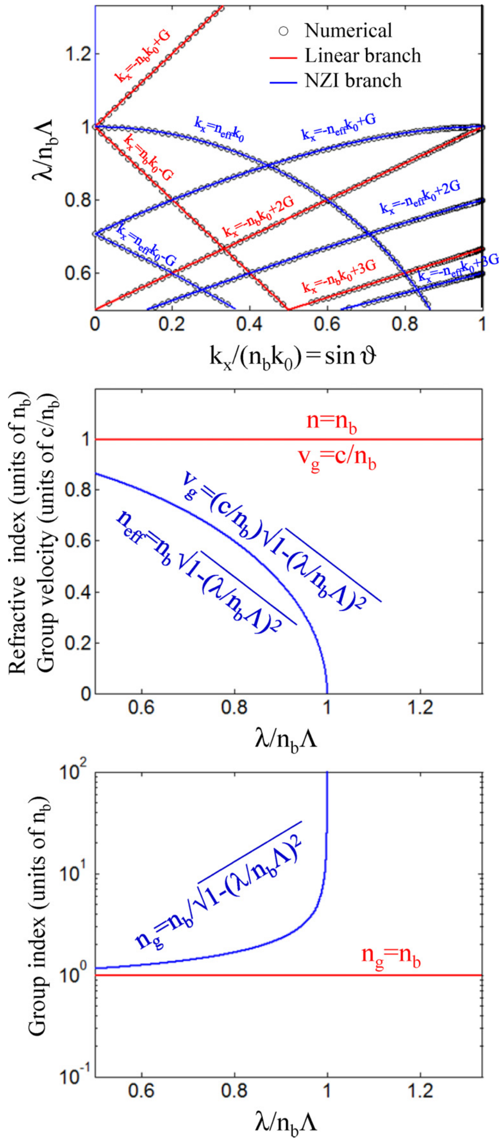

FIG. 2. (Color online) (a) Numerically calculated dispersion diagram (circles) in the momentum-wavelength plane compared with the analytically calculated linear branches (red line) and the NZI branches (blue line). The particle array is in a square lattice ($\Lambda_x = \Lambda_y = \Lambda$). The structure's parameters are $r/\Lambda = 0.1$, $\varepsilon_s = 12$, and $\varepsilon_b = 4$. (b) Effective index and group velocity vs normalized wavelength for the linear branches (red line) and for the NZI branches (blue line). (c) Same as in (b) for the group index.

$$\text{TE}: \begin{cases} E_{x,in} = 0, & E_{y,in} = E_0 e^{i(\sqrt{\varepsilon_b k_0^2 - k_{x,in}^2}z + k_{x,in}x)}, \quad E_{z,in} = 0, \\ A^{(x)}_{m,n} = -i\frac{p_y\alpha_m\beta_n}{2\varepsilon_b\Lambda_x\Lambda_y k_{m,n}}, & A^{(y)}_{m,n} = i\frac{k_0^2 p_y}{2\Lambda_x\Lambda_y k_{m,n}}\left(1 - \frac{\beta_n^2}{k_0^2\varepsilon_b}\right), \quad A^{(z)}_{m,n} = -\frac{z}{|z|}i\frac{p_y\beta_n}{2\Lambda_x\Lambda_y\varepsilon_b}, \end{cases} \qquad (2b)$$

$$\text{TM}: \begin{cases} E_{x,in} = H_0\frac{\sqrt{k_0^2\varepsilon_b - k_{x,in}^2}}{k_0\varepsilon_b}e^{i(\sqrt{\varepsilon_b k_0^2 - k_{x,in}^2}z + k_{x,in}x)}, \qquad E_{y,in} = 0, \qquad E_{z,in} = -\frac{k_{x,in}}{k_0\varepsilon_b}H_0 e^{i(\sqrt{\varepsilon_b k_0^2 - k_{x,in}^2}z + k_{x,in}x)}, \\ A^{(x)}_{m,n} = i\frac{k_0^2 p_x}{2\Lambda_x\Lambda_y k_{m,n}}\left(1 - \frac{\alpha_m^2}{k_0^2\varepsilon_b}\right) - \frac{z}{|z|}i\frac{p_z\alpha_m}{2\Lambda_x\Lambda_y\varepsilon_b}, \\ A^{(y)}_{m,n} = -i\frac{\beta_n}{2\Lambda_x\Lambda_y\varepsilon_b}\left(\frac{p_x\alpha_m}{k_{m,n}} + \frac{z}{|z|}p_z\right), \\ A^{(z)}_{m,n} = i\frac{k_0^2}{2\Lambda_x\Lambda_y}\left[-\frac{z}{|z|}\frac{p_x\alpha_m}{k_0^2\varepsilon_b} + \left(1 - \frac{k_{m,n}^2}{k_0^2\varepsilon_b}\right)\frac{p_z}{k_{m,n}}\right]. \end{cases} \qquad (2c)$$

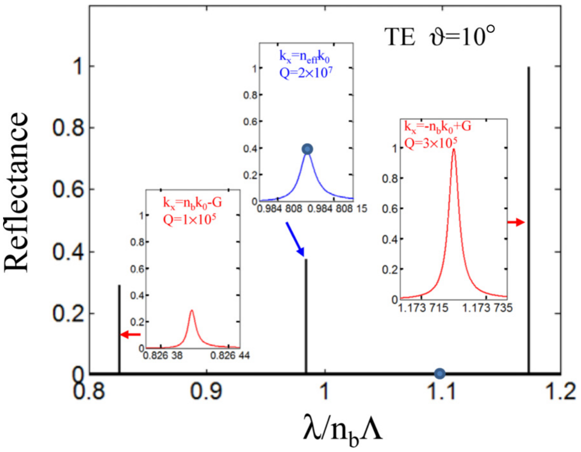

FIG. 3. (Color online) Reflectance vs normalized wavelength for TE polarization and $\vartheta = 10°$. The insets show a magnification of the reflection resonances. The right-side and left-side resonances (in red) correspond to the excitation on the linear branches with $m = \pm 1$, whereas the central resonance (in blue) corresponds to the excitation on the NZI branch with $m = 0$. The insets also report the respective Q factors of the resonances. The dot on the central resonance peak ($\lambda/n_b\Lambda = 0.984\,808\,075$) and the one out of resonance ($\lambda/n_b\Lambda = 1.1$) indicate the tuning conditions for the calculation of the fields shown in Fig. 4.

By looking at the analytical expressions of the scattered fields [Eq. (2)] and considering our particular incident conditions, consistent with the previous discussion on the absence of nondiagonal terms in the Green's tensor, it can be easily ascertained that a conversion of polarization is not possible for the fundamental (0,0) scattered mode. In other words, the polarization of the (0,0) scattered E field remains parallel to that of the incident E field along the y axis for TE polarization. Similarly, the polarization of the (0,0) scattered H field remains parallel to that of the incident H field along the y axis. Conversion of polarization may happen for the higher scattered orders, provided that they lie inside the cone of light. We will further discuss this issue for a particular case later on.

In general the array resonances correspond to the poles of Eq. (1), which are found to satisfy the condition $\mathrm{Re}(\alpha^{-1}) \cong k_0^2\mathrm{Re}[\sum G_{jj}(x_m,y_n,z=0)e^{ik_{x,in}x_m}]$ with $jj = xx, yy, zz$. For subwavelength dielectric spheres (or metallic spheres far off their intrinsic plasmonic resonance) the intrinsic particle polarizability α is very small, implying that $\mathrm{Re}(\alpha^{-1}) \gg k_b^3/(6\pi\varepsilon_b)$. Consequently, the poles are very close to the intrinsic divergences of the lattice summations, occurring at the Wood-Rayleigh anomalies of the array. By using the Poisson summation rule [13] it can be demonstrated that the lattice summations in Eq. (1) diverge as

$$\sum_{p,q} G_{jj}(x_p,y_q,z=0)e^{ik_{x,in}x_p} \propto \frac{1}{\sqrt{k_b^2-(k_{x,in}+mG_x)^2-n^2G_y^2}}, \quad jj = xx,yy,zz. \tag{3}$$

The dispersion of the array can be therefore found with good approximation under the condition that renders null the

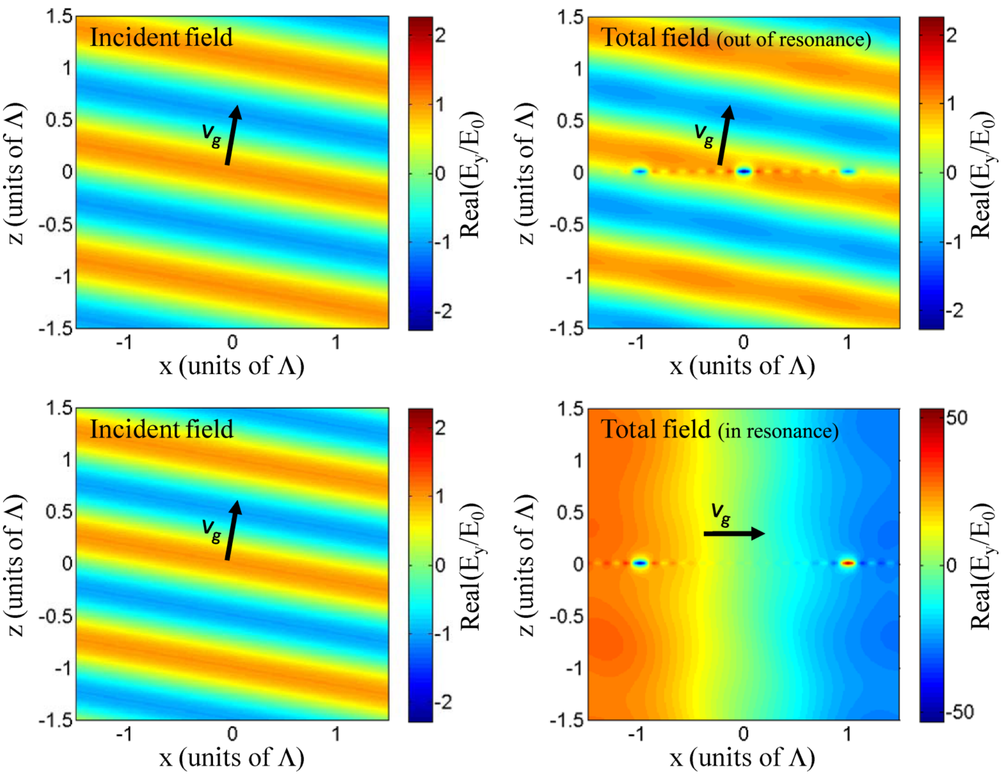

FIG. 4. (Color online) Incident field and total field (y component) out of resonance (upper panel) and in resonance (lower panel) for the tuning conditions described in the caption of Fig. 3. For an animation of the time evolution of the fields see Supplemental Material [15].

radicand in Eq. (3) which is as follows:

$$k_{x,in} = -mG_x + \mathrm{sgn}(m)\sqrt{n_b^2 k_0^2 - n^2 G_y^2}, \tag{4}$$

where $\mathrm{sgn}(m)$ is the sign of m [with the convention that $\mathrm{sgn}(0) = 1$].

Equation (4) captures the entire family of Wood-Rayleigh anomalies of the array corresponding to one of the diffracted orders becoming grazing to the plane of the array.

If we consider $n = 0$, from Eq. (4) we get $k_{x,in} = -mG_x + \mathrm{sgn}(m) n_b k_0$. In this case the group velocity of the field propagating along the plane of the array $V_g = \partial\omega/\partial k_x$ is equal to its phase velocity $V_{ph} = c/n_b$ as one may expect. Yet, another interesting condition is admitted when $n = 1$. In this case, we have $k_{x,in} = -mG_x + \mathrm{sgn}(m)\sqrt{k_b^2 - G_y^2}$. This condition can be recast in a more explicative form as $k_{x,in} = -mG_x + \mathrm{sgn}(m) n_{\mathrm{eff}} k_0$, where we have introduced the effective index of the mode propagating along the particle array plane as

$$n_{\mathrm{eff}} = n_b \sqrt{1 - \left(\frac{\lambda}{n_b \Lambda_y}\right)^2}. \tag{5}$$

The group velocity of this mode can be calculated as

$$V_g = \frac{c}{n_{\mathrm{eff}} - \lambda \frac{dn_{\mathrm{eff}}}{d\lambda}} = \frac{c}{n_b}\sqrt{1 - \left(\frac{\lambda}{n_b \Lambda_y}\right)^2}, \tag{6}$$

where c/n_{eff} is its effective phase velocity. This mode is a leaky wave for which an effective guided index and an effective group velocity can be defined along the array plane in much the same way as an effective guided index, and an effective group velocity can be assigned to conventional waveguide modes. However, since the effective index is lower than n_b, they lie within the light cone and radiate energy as they propagate along

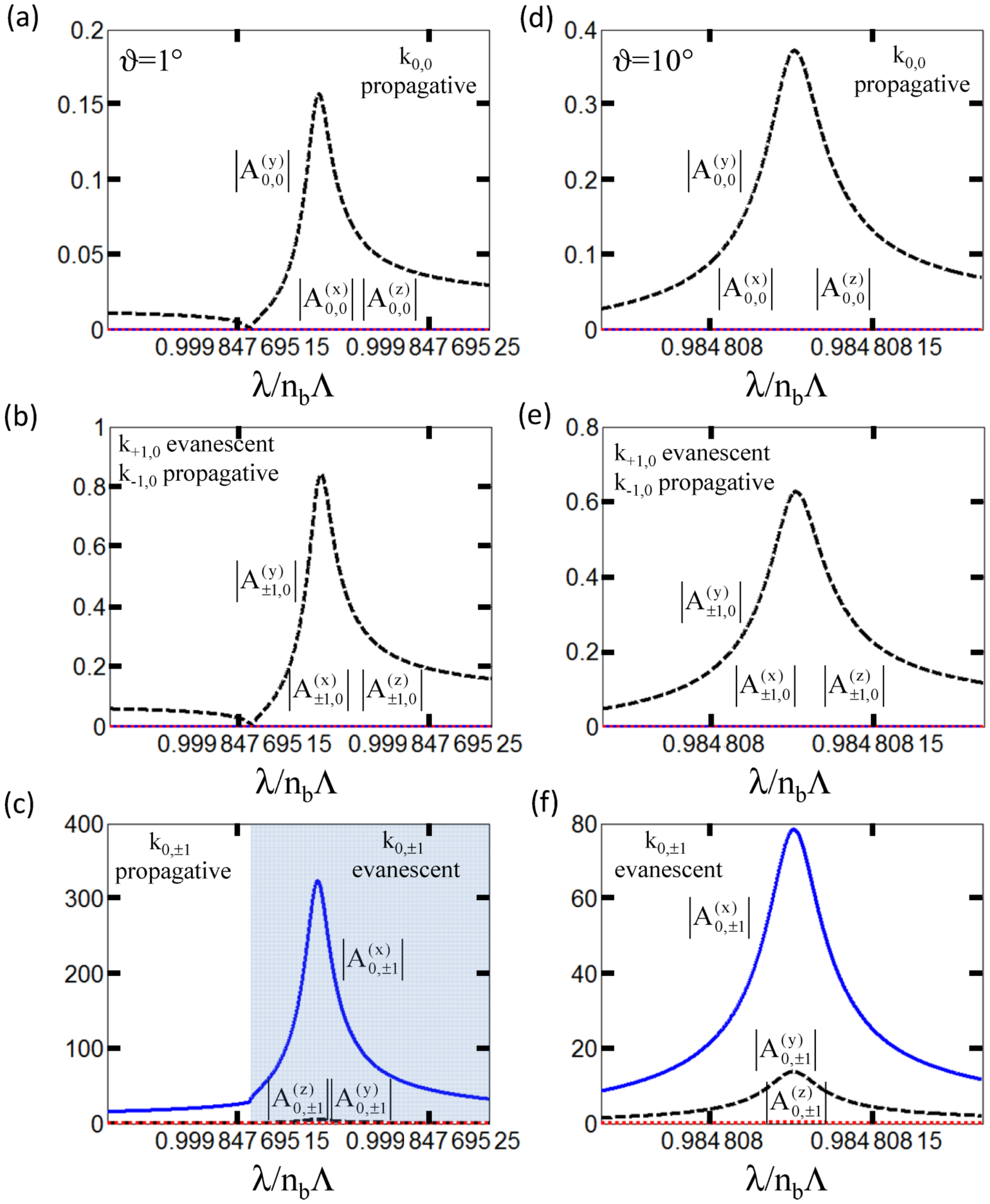

FIG. 5. (Color online) Scattering amplitudes (in units of the incident field E_0) vs normalized wavelength for the first diffracted orders.

the array plane. Their effective index effectively determines the scattering properties associated with the mode. Although a dilute single layer of subwavelength particles does not possess a refraction index "*sensu stricto*," nevertheless, the leaky wave propagating along the plane of the array "feels" an effective index lower than n_b and a close to zero group velocity as it approaches its cutoff.

Equations (5) and (6) confirm that both effective index and group velocity get close to zero near the condition $\lambda = n_b \Lambda_y$. The mode is essentially "frozen" along the plane of the array with close-to-zero group velocity and an effective transverse wavelength approaching infinity as if it were propagating across a zero-index metamaterial near its plasma frequency (in our case the effective plasma frequency is given by $\omega_p = 2\pi c/n_b \Lambda_y$). Different from conventional ε-near-zero metamaterials [9], which are metal based, here an effective zero index of propagation can be achieved with dielectric particles (or metallic particles far off their plasmonic resonance), and the response is obtained by exploiting an intrinsic lattice resonance. We note that an analogous zero-index response with sharp reflection features from a photonic crystal made of periodic apertures in a dielectric slab was reported in Ref. [14], and our theory, properly generalized to consider magnetic dipoles modeling the apertures, may be able to also capture these related phenomena. In what follows we will refer to the dispersion described by $k_{x,in} = -mG_x + \text{sgn}(m) n_b k_0$ as the "linear branches" and to the dispersion described by $k_{x,in} = -mG_x + \text{sgn}(m) n_{\text{eff}} k_0$ as the "near-zero index (NZI) branches."

As an example, in Fig. 2(a) we show the numerically calculated dispersion branches in comparison with the analytical ones, i.e., the linear branches and the NZI branches, for a structure whose parameters are specified in the figure caption. Figures 2(b) and 2(c) show the corresponding effective index, group velocity, and group index ($n_g = c/V_g$). The numerically calculated dispersion curves follow almost exactly the analytical ones, confirming our theoretical analysis.

In Fig. 3 we show the calculated TE reflectance (R) of the array (reflected power normalized to the incident power over an elementary cell with all the diffraction orders taken into account) vs normalized wavelength for $k_x/n_b k_0 = \sin(10^\circ)$, i.e., for an incident angle $\vartheta = 10^\circ$. The reflectance is calculated as $R = \sum_{m,n} R_{m,n}$, where $R_{m,n}$ is the reflectance associated with the (mth,nth) diffracted order and (m,n) run only over the propagative modes, i.e., the modes for which $\text{Im}(k_{m,n}) = 0$. As the incident angle decreases toward the near-to-normal incidence condition, the three resonances converge to the same spectral position, determined by $\lambda = n_b \Lambda$.

In Fig. 4 we show a snapshot of the incident field and the y component of the total field out of resonance (upper panel) and in resonance on the NZI branch (lower panel) as indicated in Fig. 3. For an animation of the time evolution of the fields see Ref. [15]. The figure enlightens several important features: Out of resonance (upper panel) the scattering cross section is minimal as one would expect from an array of sparse subwavelength nonresonant particles. The total field (right) shows just minimal distortions compared to the impinging

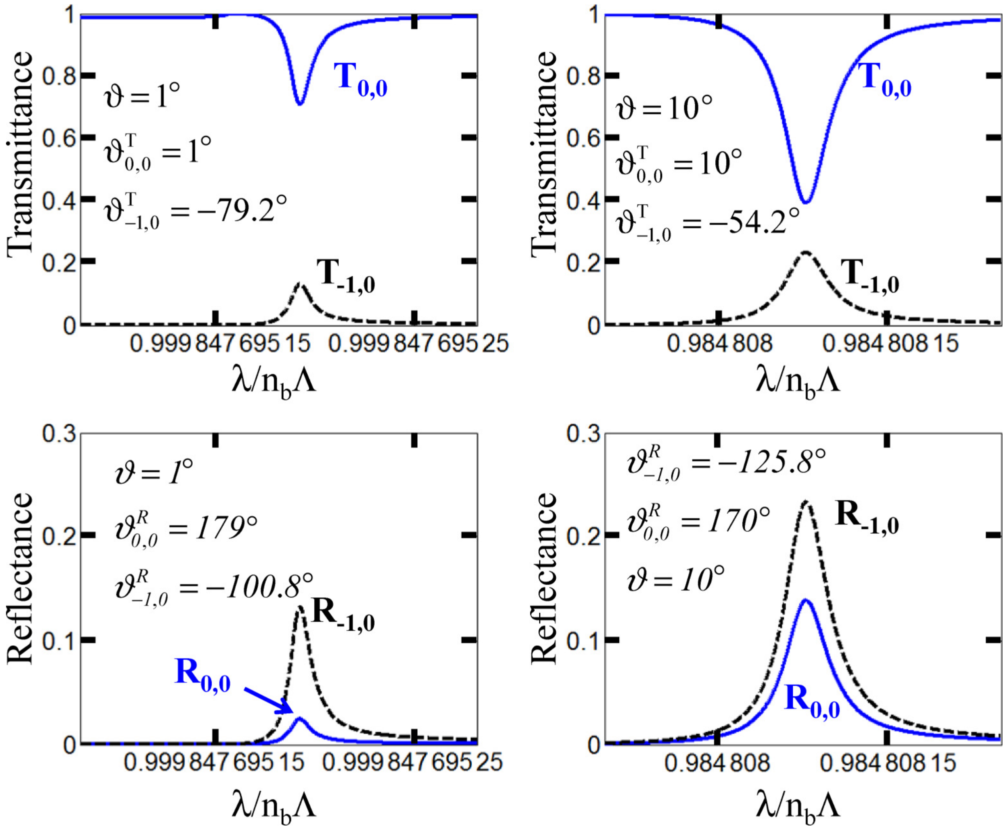

FIG. 6. (Color online) Reflectance and transmittance vs normalized wavelength for the propagative scattering orders for an incident angle of $\vartheta = 1^\circ$ (left panel) and $\vartheta = 10^\circ$ (right panel).

field (left). At resonance (lower panel), the total field is resonantly enhanced with respect to the incident field (note the different scales in the lower panels), and its propagation becomes essentially parallel to the plane of the array.

In Fig. 5 we show the relative strength (in units of the incident field E_0) of the first scattered orders, (0,0), (0,±1), and (±1,0), respectively, on the NZI branch for an incident angle $\vartheta = 1°$ [(a)–(c), left panel] and $\vartheta = 10°$ [(d)–(f), right panel]. In the figures we also specify the propagative and evanescent scattering orders. The first are characterized by a purely real wave vector along the z axis [$\mathrm{Im}(k_{m,n}) = 0$] and can propagate electromagnetic power into the far field, the latter, admitting an imaginary part of the wave vector, lie outside the cone of light, i.e., basically they are confined in the near field close to the plane of the array just propagating along the plane itself and are associated with only reactive power [13].

In Fig. 6 we calculate the power transmitted/reflected by the propagative diffraction orders and their respective scattering angles.

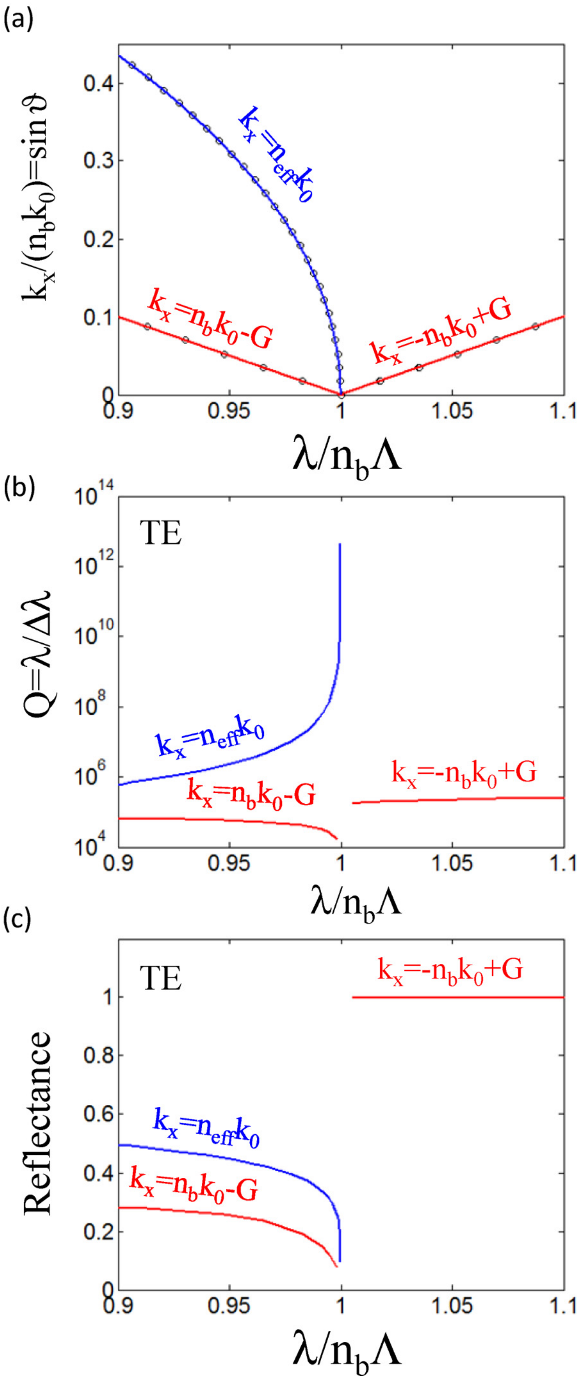

FIG. 7. (Color online) (a) Dispersion in the wavelength-momentum plane close to the condition $\lambda/n_b\Lambda = 1$. Q factor [Fig. 7(b)] and reflectance [Fig. 7(c)] of the resonances vs normalized wavelength along the two linear branches (red lines) and along the NZI branch (blue line).

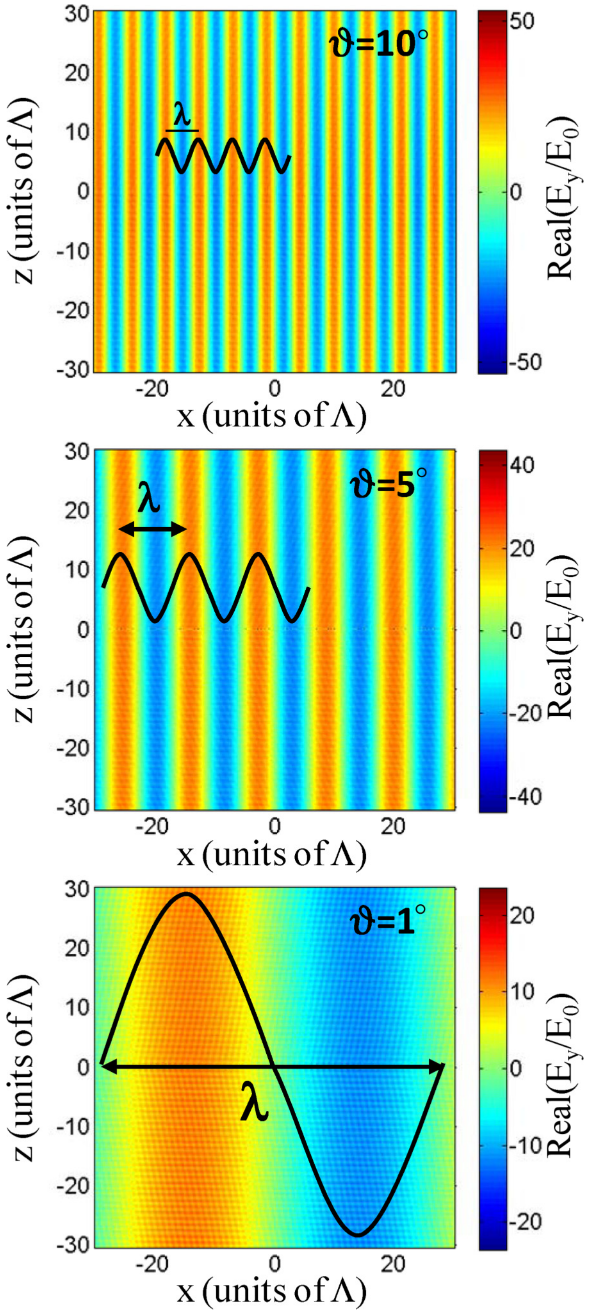

FIG. 8. (Color online) Electric field on the NZI branch for different incident angles.

From Figs. 5 and 6 several important considerations can be drawn. First, it is seen that only the (0,0) and the (−1,0) diffracted orders propagate into the far field. At resonance, the power backscattered from the array for the incident angle $\vartheta = 10°$ is ∼15% for the (0,0) mode and ∼25% for the (−1,0) mode, respectively, for backscattered angles of 170° and −125.8°, respectively. For the incident angle $\vartheta = 1°$, the power backscattered is ∼3% and ∼15%, respectively, for backscattered angles of 179° and −100.8°, respectively. Note that here we refer to the angle between the positive z axis and the k vector of the incident reflected or transmitted wave. The angles are considered positive if taken counterclockwise, negative if taken clockwise. Second, the field components associated with the far-field scattering essentially conserve the incident field polarization as is seen from Fig. 5 where the y-polarized scattering amplitudes are the only nonzero amplitudes associated with the (0,0) and the (−1,0) scattering modes. An interesting behavior characterizes instead the near-field (evanescent) components of the scattering process. In this case, the amplitudes of the x-polarized and y-polarized scattered fields show a resonant response with extremely high local field enhancements [see in particular Fig. 5(f) where on resonance we have that $|A_{0,\pm1}^{(x)}| \sim 80E_0$ and $|A_{0,\pm1}^{(y)}| \sim 20E_0$ at $\vartheta = 10°$], indicating large stored energy. These components dominate the near-field dynamics. Note, incidentally, that in Fig. 4 and in the Supplemental Material's related animation [15] the y component of the total resonant field is dominated by $A_{0,\pm1}^{(y)}$. For close-to-normal incidence the y-polarized near-field component becomes less effective, whereas the x component is largely increased, and the relative resonance acquires a typical Fano-like shape with remarkably high values of the local field enhancement [see Fig. 5(c) where we have that $|A_{0,\pm1}^{(x)}| \sim 300E_0$]. This exceptionally high value of the local field is also accompanied by a transition from the evanescent to the propagative mode on the high-frequency tail of the Fano resonance, although the power backscattered in the far field, thanks to this transition, is less than 1%. In Fig. 7 we monitor how the three resonances vary as the incident angle is decreased. In particular we calculate the Q factor ($Q = \lambda/\Delta\lambda$) and the maximum reflectance of these resonances along the two linear branches with $m = \pm1$ and along the NZI branch with $m = 0$. Close to the condition $\lambda/n_b\Lambda = 1$, the Q factor of the NZI branch peaks exceedingly high values above 10^{10}. The increase in Q factor is accompanied by a decrease in the resonance amplitude as can be seen from Fig. 7(c), which could make them hardly detected under ordinary experimental conditions.

The reflectance at these resonances also provides an estimate of the fraction of incident power coupled to the array. In Fig. 8 we show three snapshots of the electric field on the NZI branch for different incident angles, namely, $\vartheta = 10°$, $\vartheta = 5°$, and $\vartheta = 1°$, consistent with the results in the bottom panels of Fig. 4. It is seen how the field strength decreases as the incidence angle gets closer to normal, whereas at the same time the effective wavelength along the plane of the array sensibly increases.

For completeness, in Fig. 9 we also show the fields in the plane of the array at $z = 0$ calculated along the NZI branch

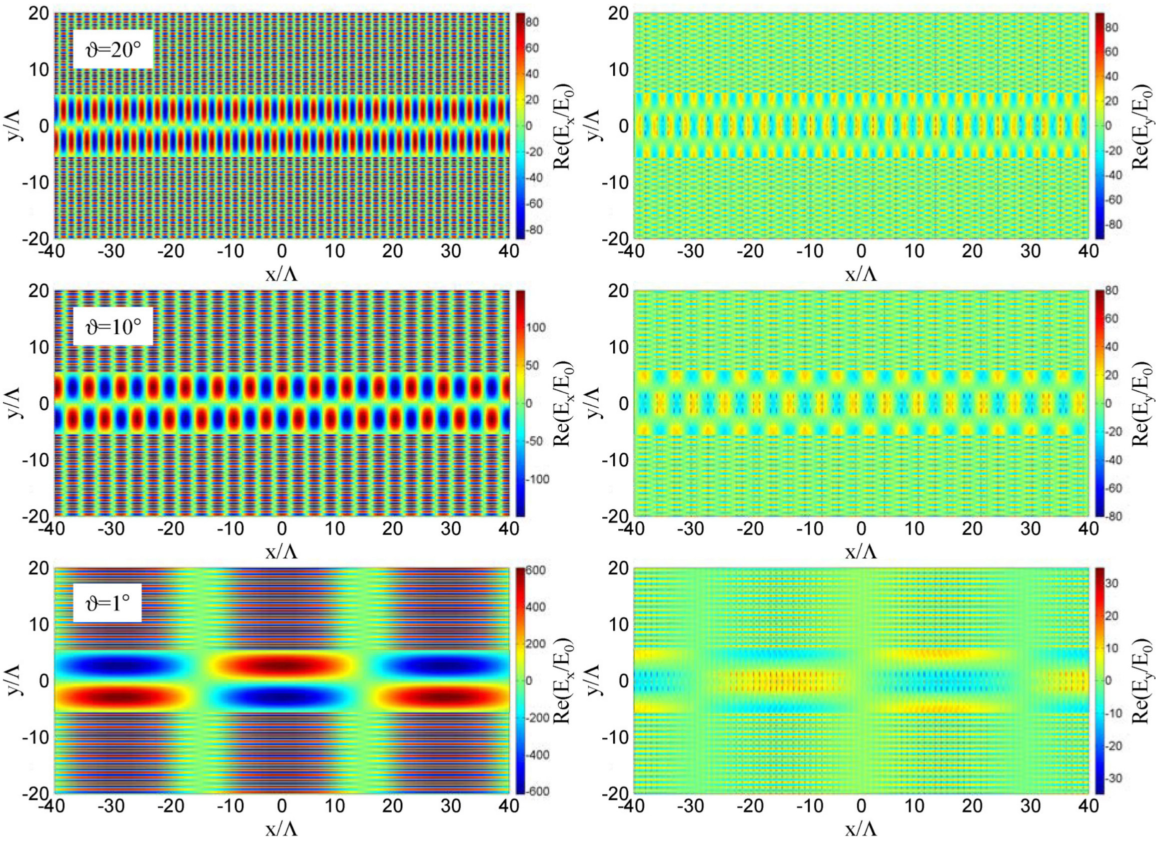

FIG. 9. (Color online) Electric field in the plane of the array at $z = 0$ for different incident angles.

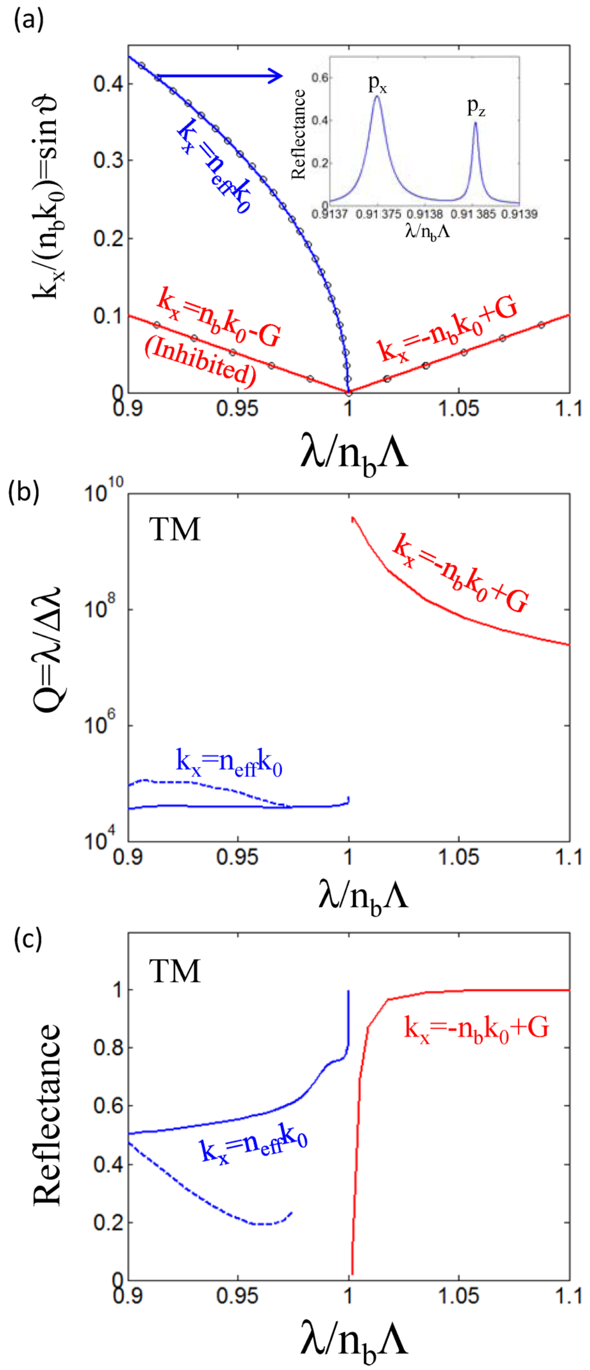

FIG. 10. (Color online) Same as Fig. 7, but for TM polarization. The inset of (a) shows the two-peaked reflectance due to the excitation of the p_x and p_z dipole components. In (b) and (c) the continuous and dashed blue lines, respectively, refer to the resonances induced by p_x and p_z. The solid lines in Figs. 7(a) and (a) are the same.

for different incident angles. The fields are obviously periodic along the y direction with periodicity given by Λ. For a better visualization of the field properties, a magnification of the field along the x axis and one elementary cell along y is also superimposed.

In Fig. 10 a study similar to Fig. 7 is provided for TM polarization of the incident light.

For the TM case, one of the linear branches is inhibited due to the fact that the induced dipole moments p_x and p_z calculated through the Ewald procedure are close to zero on this branch. The NZI branch is characterized by a Q factor lower than the corresponding TE branch. Also, reflectance for off-normal incidence shows a typical two-peaked shape due to the simultaneous excitation of x and z components of the dipole moment as shown in the inset of Fig. 10(a). Besides the lower Q factor, the frozen light branch for TM polarization also shows more pronounced resonances (which indicates a better coupling efficiency with the array's surface), properties that may make them more easily detected in an experiment. For this reason, we have performed a preliminary experimental verification of the existence of the NZI branch in the microwave regime for TM polarization as detailed in the next section.

III. EXPERIMENTAL RESULTS

Steel spheres ($2r = 4.5$ mm) have been inserted into an extruded polystyrene foam sheet (62 cm × 30 cm × 5.5 mm) to form a square array with 16-mm periodicity as shown in Fig. 11(a).

Using an rf Agilent (E8363C) vector network analyzer, the sample transmittance as a function of angle was measured. Figure 11(b) shows the analytical dispersion (continuous lines) calculated according to Eq. (4) and the measured dispersion along the NZI branch (dots) for TM polarization. The agreement is overall very good. The metal spheres are almost completely embedded in foam and extend above its surface by 0.5 mm. In the theoretical calculation we made the assumption that the metal spheres are fully immersed in a medium with refractive index $n_b = 1.04$ as retrieved from separate measurements of an isolated foam block.

Figures 11(c)–11(e) give an example of the measured transmittance of the (0,0) mode through the array along the NZI branch for different incident angles. We note that the spectral position of the resonance is well captured by the model, although in the experiment the resonance bandwidth is much broader than what is predicted by the theory. The quality factor of the measured resonances is $Q \sim 38$, much smaller than the one predicted by our model, which, using a Debye material for the steel $\varepsilon_s = 1 + i\sigma/(2\pi\varepsilon_0\omega)$ with $\sigma = 1.45 \times 10^6$ S/m, would predict a quality factor $Q \sim 1700$.

This reduction in Q factor is expected due to the finite size of the array, which hampers the transverse energy buildup of the resonance. Given our particular incident conditions ($k_{y,\mathrm{inc}} = 0$), the energy buildup associated with the resonance is due to the constructive interference of the scattered fields along the x direction. In our case the array dimension along the x direction measured in units of incident wavelength is $\sim 62/1.6$ cm ~ 38, which coincides with the experimentally measured Q factor. We also remark that in our case the refractive index of the foam is very close to that of the free space, therefore its presence should not be considered a plausible cause for the reduction of the resonance Q factor as instead it would be the case for higher index contrast substrates [16]. Narrower resonances approaching the theoretical calculated limit may be achieved by enlarging the array size. Of course,

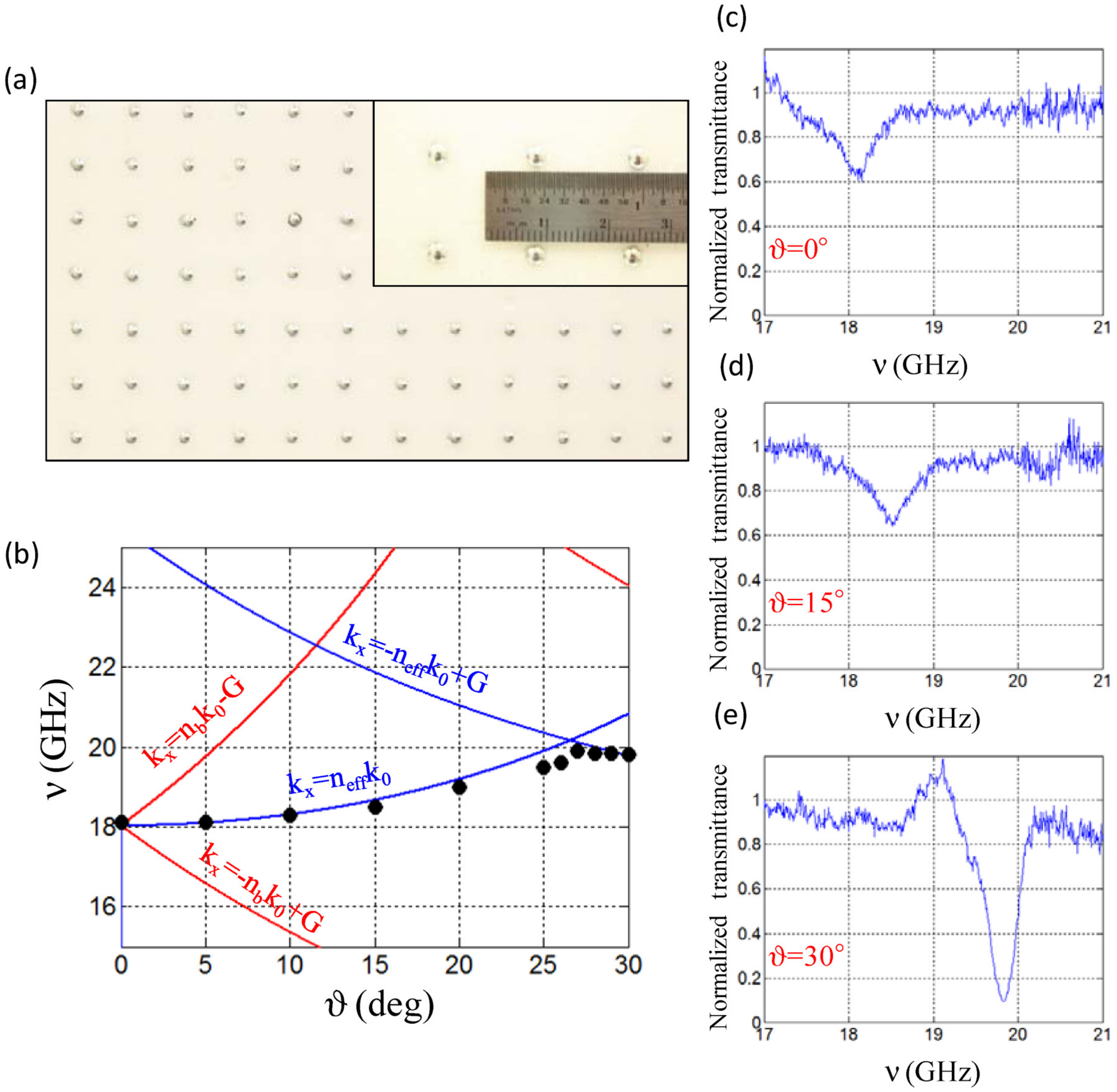

FIG. 11. (Color online) (a) Photograph of the sample. Steel spheres (4.5-mm diameter) have been inserted into an extruded polystyrene foam sheet (62 cm × 30 cm × 5.5 mm) to form a square array with $\Lambda = 16$ mm. (b) Calculated dispersion (continuous line) in the (ν,ϑ) plane and measured dispersion (dots) along the NZI branch for TM polarization. (c)–(e) Measured resonances for different incident angles. Transmission was measured between two horn antennas placed on the two sides of the metasurface (actual level of the transmission measurements are shown on the vertical axis, normalized to the case without a sample). In this case only the transmittance of the (0,0) mode has been collected.

whereas this could be impractical in the microwave regime due to the extremely large sample dimensions, it is actually within the capability of the current lithographic technique in the visible and IR. We predict that with larger arrays and more precise fabrication tools as using photonic crystal technology [14], it can be possible to experimentally verify extremely large Q factors and the frozen light at the NZI branch in the visible and IR.

IV. CONCLUSIONS

In conclusion, we have analyzed light propagation across a planar array of weak and sparse subwavelength scatterers and have shown that collective lattice resonances are able to produce light modes propagating along the plane with zero effective index and zero group velocity. Our results may provide insight into the anomalous scattering features from periodic arrays near normal incidence and may provide significant enhancement for nonlinear optical interactions, biosensing, optical storage, and quantum information processing. For example, by properly tailoring the dispersion properties of the structure in a quadratic background medium, it may be possible to obtain phase and group-velocity matching for second-harmonic generation. For a Kerr-like background medium, we may envision efficient all-optical switching based on this principle, possibly integrated in an optical fiber. The remarkably high field localization on the plane of the array makes this structure also ideal for studying surface-enhanced Raman scattering. Other applications may include delay lines for signal processing and quantum information processing.

[1] R. Boyd, J. Opt. Soc. Am. B **28**, A38 (2011).

[2] L. V. Hau, S. E. Harris, Z. Dutton, and C. H. Behroozi, Nature (London) **397**, 594 (1999).

[3] M. M. Kash, V. A. Sautenkov, A. S. Zibrov, L. Hollberg, G. R. Welch, M. D. Lukin, Y. Rostovtsev, E. S. Fry, and M. O. Scully, Phys. Rev. Lett. **82**, 5229 (1999).

[4] A. V. Turukhin, V. S. Sudarshanam, M. S. Shahriar, J. A. Musser, B. S. Ham, and P. R. Hemmer, Phys. Rev. Lett. **88**, 023602 (2001).

[5] T. Baba, Nat. Photonics **2**, 465 (2008).

[6] G. D’Aguanno, M. Centini, M. Scalora, C. Sibilia, M. Bertolotti, E. Fazio, C. M. Bowden, and M. J. Bloemer, Phys. Rev. E **68**, 046613 (2003).

[7] G. D’Aguanno, N. Mattiucci, M. Scalora, M. J. Bloemer, and A. M. Zheltikov, Phys. Rev. E **70**, 016612 (2004).

[8] G. D’Aguanno, N. Mattiucci, and M. J. Bloemer, J. Opt. Soc. Am. B **25**, 1236 (2008).

[9] R. Liu, Q. Cheng, T. Hand, J. J. Mock, T. J. Cui, S. A. Cummer, and D. R. Smith, Phys. Rev. Lett. **100**, 023903 (2008); B. Edwards, A. Alù, M. E. Young, M. Silveirinha, and N. Engheta, *ibid.* **100**, 033903 (2008).

[10] F. J. Garcia de Abajo, Rev. Mod. Phys. **79**, 1267 (2007).

[11] B. T. Draine, Astrophys. J. **333**, 848 (1988).

[12] K. Jordan, G. Richter, and P. Sheng, J. Comput. Phys. **63**, 222 (1986).

[13] R. E. Collins, *Field Theory of Guided Waves*, IEEE Press Series on Electromagnetic Wave Theory (Wiley, New York, 1991).

[14] J. Lee, B. Zhen, S.-L. Chua, W. Qiu, J. D. Joannopoulos, M. Soljacic, and O. Shapira, Phys. Rev. Lett. **109**, 067401 (2012).

[15] See Supplemental Material at http://link.aps.org/supplemental/10.1103/PhysRevB.90.054202 for a movie on the time evolution of the field out of resonance and in resonance.

[16] B. Auguié, X. M. Bendaña, W. L. Barnes, and F. J. García de Abajo, Phys. Rev. B **82**, 155447 (2010).